Journal of Molecular Catalysis A: Chemical 348 (2011) 1–13

Contents lists available at ScienceDirect

Journal of Molecular Catalysis A: Chemical

journal homepage: www.elsevier.com/locate/molcata

Nanocasted oxides for oxidative dehydrogenation of ethylbenzene utilizing CO_2 as soft oxidant

Samuel P.D. Marques[a,1], Anderson L. Pinheiro[a,1], Tiago P. Braga[a,1], Antoninho Valentini[a,1], Josue M. Filho[b,2], Alcineia C. Oliveira[a,*]

[a] Universidade Federal do Ceará, Campus do Pici-Bloco 940, Departamento de Química Analítica e Físico Química, Langmur Lab. de Adsorção e Catálise, Fortaleza, Ceará, Brazil
[b] Universidade Federal do Ceará, Campus do Pici-Bloco 922, Departamento de Fisica, Fortaleza, Ceará, Brazil

ARTICLE INFO

Article history:
Received 12 April 2011
Received in revised form 12 July 2011
Accepted 26 July 2011
Available online 4 August 2011

Keywords:
Oxides
Styrene
Nanocasting
Ethylbenzene
Raman studies

ABSTRACT

Nanocasted oxides were evaluated in the production of styrene via the dehydrogenation of ethylbenzene utilizing CO_2 as soft oxidant. Mesoporous binary and ternary oxides catalysts were obtained by nanocasting polymeric beads, as a mold. The chemical and structural properties of the solids were characterised by SEM–EDX, TEM, nitrogen adsorption measurements, TPR, CO_2-TPD, Raman and FTIR analyses. The solids were evaluated in dehydrogenation of ethylbenzene utilizing CO_2 as soft oxidant. XRD analyses indicated that the structures of CeFeCo, CeFeZr, CeFeNi and CeNiAl were more crystalline than that of CeFe, SnFe and MnFe. SEM and TEM analyses suggested that the replication strategy allowed CeNiAl, CeFe, MnFe and CeFeCo composites to retain the textural and structural properties of the mold. CO_2-TPD analysis of the solids revealed that basic sites of medium to high strengths were present in the ternary solids. The textural properties were related to the crystal structure and morphology of the catalysts. Moreover, the reducibility of the solids was highly dependent on their structures. Thus, ternary composites were stabilised by phases with low reducibility, and the activity of the catalysts was enhanced. For instance, CeFeCo possessing a mesostructured feature and a highly stable $CoFe_2O_4$ spinel phase showed superior catalytic activity for the production of styrene (conversion = 25%; selectivity for styrene = 45%) at 550 °C. Alternatively, CeFe, SnFe, MnFe, CeFeZr, CeFeNi and CeNiAl displayed modest activity in the dehydrogenation of ethylbenzene. At temperatures greater than 550 °C, the catalytic performance of the CeFeCo catalyst was improved but coking decreased the selectivity. The catalytic performance of the CeFeCo catalyst was comparable to those of traditional iron oxide catalysts used in the dehydrogenation of ethylbenzene.

1. Introduction

Due to the increasing demands of energy and concerns with environment protection, efficient production and use of clean energy have become particularly important. Thus, over the last few decades, great attention has been paid to the oxidative dehydrogenation of ethylbenzene (ODH) from the perspective of the effective utilization of CO_2 as a mild oxidant to produce value added products. The ODH is an alternative to steam-based dehydrogenation to produce styrene [1–7]. Styrene, an important chemical intermediate, is widely used as a feedstock for the production of polymers. Industrially, the dehydrogenation of ethylbenzene with steam is the main route for the synthesis of styrene [1–5]. However, high reaction temperatures (i.e., 600–700 °C) and excessive amounts of superheated steam result in an equilibrium-limited and energy-demanding process [1–4].

ODH avoids the aforementioned thermodynamic limitations of the current industrial process, including energy loss and catalyst deactivation [5–12,13]. Various oxidising agents such as oxygen, sulphur dioxide, dry air, carbon dioxide and dinitrogen oxide have been used in ODH [6–9]. Carbon dioxide is a soft oxidant that possesses several advantages over the aforementioned oxidants. For instance, with CO_2, latent heat is not lost from the reaction because CO_2 remains in the gaseous state throughout the reaction [5–8,14]. Moreover, CO_2 can be used at low reactant partial pressures and has the highest heat capacity among various gases [10,2]. In addition, CO_2 minimises the production of hydrocarbons, which can lead to the generation of carbon oxides. In the dehydrogenation of ethylbenzene with CO_2, the latter gas is consumed rather than produced. Indeed, CO_2 can be used in the coupling of reverse water-gas

* Corresponding author. Tel.: +55 85 3366 9051; fax: +55 85 3366 9051.
E-mail address: alcineia@ufc.br (A.C. Oliveira).
[1] Tel.: +55 85 3366 9051; fax: +55 85 3366 9051.
[2] Tel.: +55 85 3366 9900; fax: +55 85 3366 9900.

1381-1169/$ – see front matter © 2011 Elsevier B.V. All rights reserved.
doi:10.1016/j.molcata.2011.07.013

shifts and simple dehydrogenation reactions [11]. Because of the endothermicity of the reaction, CO_2 can be used for the storage of chemical energy.

Many investigations on the dehydrogenation of ethylbenzene with CO_2 over transition metal oxides have been reported [6–8]. Iron-based catalysts have been used for the production of styrene because they are relatively cheap and possess high activity [3,5–7,11]. However, iron based catalysts quickly deactivate in ODH due to sintering of the active metal phase and coke deposition. Studies have shown that nanocasted oxides have been successfully applied to the dehydrogenation of ethylbenzene with CO_2; however, their activity and stability depends on the active components of the catalyst [13].

Nanocasting techniques are attractive alternatives for the synthesis of nanosized inorganic materials [15–19]. The structure and surface properties of nanocasted oxides have a significant effect on the catalytic activity in the reactions that they were tested [19–27]. These oxides possessing high activity and greater stability are suitable catalysts that could provide larger external surface areas and shorten the diffusion distances in the channels of the particles [20,21], thus facilitating access to the active sites and reducing deactivation, commonly found in the conventional oxides. Particularly in the catalysts for styrene production via ODH, the low resistance to deactivation is still the major drawback for the use of the conventional catalysts solids in dehydrogenation of ethylbenzene reactions, as aforesaid. Therefore, the search for new oxide catalysts remains a priority. The catalytic activities of the metal oxides have been recently explored.

Because of the stability of nanocasted oxides, as well as their ability to generate active sites and to store and transport oxygen, nanocasted oxides can increase the surface area of the catalysts, and enhance their performance [20]. In addition, binary iron and ternary iron-based oxides may improve the performance of the catalysts by increasing the stability of the solids [19–34]. Thus, to apply nanocasted metal oxides to the dehydrogenation of ethylbenzene with CO_2, a catalyst that is resistant to carbon deposition and exhibits stable activity over time on stream must be developed. Therefore, the aim of the present work is to study the influence of the structure of nanocasted oxides on the dehydrogenation of ethylbenzene to styrene.

Among an extensive range of metal oxide catalysts, CeO_2 has demonstrated to be a potential catalyst for catalytic reverse water-gas shift reaction [1,33,34]. Its excellent activity for coupling between reverse water-gas shift ($CO_2 + H_2 \leftrightarrow CO + H_2O$) and ethylbenzene dehydrogenation reaction ($C_6H_5CH_2$-$CH_3 \rightarrow H_2 + C_6H_5CH{=}CH_2$) becomes the process more favourable. Also, previous works have demonstrated that tin and manganese addition have provide thermal stability to the iron based catalyst [4]. This strongly suggests that the influence of these promoters must be discussed in detail to explain which type of metals species act in the dehydrogenation of ethylbenzene with CO_2. For a deep understanding and improvement of styrene production, binary iron based nanocasted oxides were obtained.

Additionally, since iron promoted by ceria and other components (tin, cobalt, zirconium, manganese) used for simple dehydrogenation process [3,4] work efficiently in the presence of steam, this has motivated the evaluation of carbon dioxide on these catalysts systems. Moreover, nickel aluminates have been shown an improved catalytic performance for styrene production [12]. Thus, it is reasonable that nanocasted nickel aluminate is expected to provide enhanced performance as catalyst for dehydrogenation of ethylbenzene reaction. In this work, we have also explored the possibility of synthesising ternary ceria, nickel and aluminium based catalysts using a nanocasting procedure with mesoporous XAD-16 resin, as a template. Therefore, effect of ternary iron based catalysts is discussed herein.

2. Experimental

2.1. Catalysts preparation

Catalysts were prepared via nanocasting, according to the method described in the literature [18,28,34], with modifications. To synthesise the resin template, 10 g of XAD-16 polystyrene beads (Aldrich) were dispersed into 40 mL of water for 10 min. The procedure was repeated seven times until the solution reached a pH of 7. The resulting resin was stored in distilled water.

Separately, cerium nitrate ($(NH_4)_2Ce(NO_3)_6$, Aldrich) and iron nitrate ($Fe(NO_3)_3{\cdot}9H_2O$, Vetec) were dissolved individually in deionised water, and appropriate volumes of the solutions were combined to obtain an oxide concentration of 0.5 mol. Subsequently, the mixed solutions of cerium and iron were added to 10 mL of the beads, and the resultant mixture was stirred for 30 min. Excess solvent was removed by evaporation at 60 °C for 50 h.

The resulting material was calcined at 500 °C in air at a heating rate of 2 °C min^{-1} for 8 h. The impregnation step was repeated twice to completely fill the resin. The material was once again calcined at 500 °C for 12 h in air at a heating rate of 2 °C min^{-1} for 8 h. The resulting sample was labelled as CeFe. Binary SnFe and MnFe oxides were obtained from manganese nitrate and tin chloride, respectively ($Mn(NO_3)_3{\cdot}6H_2O$, Aldrich) and ($SnCl_6.6H_2O$, Aldrich). Appropriate amounts of each reagent were used so as to yield a $(Me_1)/(Me_1 + Me_2)$ percentage of 0.5 in the final product, with Me_1/Me_2 molar ratio of 1:1.

Ternary CeFeZr, CeFeCo, CeFeNi and CeNiAl were also obtained through the aforementioned method. To prepare ternary nanocasted oxides, cobalt nitrate ($Co(NO_3)_3{\cdot}6H_2O$, Aldrich), aluminium nitrate $Al(NO_3)_3{\cdot}9H_2O$, nickel nitrate ($Ni(NO_3)_3{\cdot}6H_2O$, Synth), and zirconium oxichloride ($ZrOCl_2{\cdot}8H_2O$, Aldrich) were used as the source of metal. To obtain the final crystalline structure, the materials were calcined at 600 °C under a flow of air at a rate of 2 °C min^{-1} for 8 h. The theoretical molar ratios of the metals were 1:1:1.

2.2. Characterisation

Inductively coupled plasma optical emission spectroscopy (ICP-OES) was used to determine the concentration of metals in the catalysts. The samples were dissolved in a mixture of hydrochloric and nitric acid, and were heated in a sand bath at 200 °C. The solvent was evaporated, and nitric acid and water were added to the resulting precipitate. The analyses were conducted on a Perkin Elmer, Cary AA spectrometer.

X-ray diffraction (XRD) patterns were colleted on a DMAXB Rigaku diffractometer using CuKα radiation at 40 kV and 25 mA. The experiments were performed at high diffractions angles (from 10 to 80°). The crystallite sizes were estimated from XRD patterns calculated using Scherer's algorithm [21].

BET measurements were recorded on a Micromeritics ASAP 2002 instrument. The samples were degasified at 150 °C, and the textural features were studied via nitrogen adsorption at 77 K. The pore sizes were obtained from the analysis of the adsorption isotherms, according to the BJH method (Barrett–Joyner–Halenda).

Temperature programmed reduction (TPR) studies were performed using homemade equipment with a TCD detector. In all of the experiments, 5 vol% H_2 in N_2 was used as the reducing gas, and the gaseous mixture was passed through a 13× molecular sieve to remove water. The experiment was conducted between 50 and 1000 °C at a constant flow rate of 30 mL min^{-1}. In each experiment, 0.30 g of powdered catalyst was analysed.

The temperature programmed desorption of CO_2 (CO_2-TPD) was conducted in a homemade instrument at a nitrogen flow rate of 50 mL min^{-1}. Prior to CO_2 adsorption, all catalysts were heated to

300 °C. The samples were cooled to 60 °C and were exposed to a flow of CO_2 for 1 h. Desorption was achieved by heating the sample (10 °C min^{-1}) to a final temperature of 950 °C. Approximately 0.30 g of powdered catalyst was used to perform the analysis.

The composition of the samples was determined by energy dispersive X-ray spectroscopy (EDX) analysis using a JEOL JEM-2010 electron microscope equipped with an EDX Link Analytical QX-20000 system coupled to an SEM microscope with an acceleration voltage of 200 kV.

FTIR spectra of the spent samples were collected on a Netzsch spectrometer between 4000 and 400 cm^{-1}. Prior to the analyses, approximately 1 wt% of each sample was dissolved in KBr.

TGA measurements for spent CeFeCo catalyst were carried out using Netzsch STA 409 PC/PG equipment coupled to a Bruker Tensor 27 IR instrument. The analyses were performed on spent CeFeCo catalyst to know the coking degree of the spent sample from room temperature to 1000 °C at 10 °C min^{-1}, under air flow by placing approximately 100 mg of the sample in an aluminium pan.

Raman spectra of selected spent samples were obtained using a confocal micro-Raman spectrometer (T64000 Jobin Ivon spectrometer). An Ar laser (514.5 nm) operated at 2 mW was used as the excitation source. The laser was focused on powdered spent samples, which were placed on a microscope slide, to produce a spot with a diameter of approximately 8 mm. An air-refrigerated charge-coupled device (CCD) was used as the detector.

2.3. Catalytic measurements

The dehydrogenation of ethylbenzene by carbon dioxide was conducted in a quartz reactor equipped with a thermocouple. The reactant mixture was composed of carbon dioxide and ethylbenzene in a 30:1 ratio, respectively. The flows used were N_2: 11.7 mmol h^{-1}; CO_2: 58 mmol h^{-1}; EB: 1.98 mmol h^{-1}(CO_2/EB ratio = 30). Previously, nanocasted oxides (50 mg) were crushed and activated *in situ* under a flow of nitrogen from room temperature to 550 °C over the course of 1 h to remove gaseous impurities from the surface of the catalyst. The reaction was conducted at atmospheric pressure, 550 °C and a CO_2/EB molar ratio of 30. Every 30 min, the effluents were analysed by gas chromatography using a Simple Chrom chromatograph equipped with a FID detector. The catalytic performance was evaluated in terms of the conversion of ethylbenzene and the selectivity for styrene production, according to the following equations:

$$\%\,\text{EB conversion} = \frac{\text{EB}_{\text{in}} - \text{EB}_{\text{out}}}{\text{EB}_{\text{in}}} \times 100 \quad (1)$$

The selectivity of the reaction was based on the conversion of ethylbenzene:

$$\%\ \text{selectivity to styrene} = \frac{\text{mols of styrene produced}}{\text{mols of reacted ethylbenzene}} \times 100 \quad (2)$$

The ethylbenzene conversion and styrene selectivity were expressed as mol.% on the basis of carbon atoms, as suggested by the findings [14]. Activities were measured as mols of ethylbenzene consumed per gram of catalyst per hour and were expressed in mol g^{-1} h^{-1}. A long-term stability study was conducted to determine the catalytic performance of the most active catalyst at different temperatures.

3. Results and discussion

3.1. Chemical, structural and morphological properties of the catalysts

The chemical composition determined by ICP-OES analysis is close to 50 mol % for binary oxides (e.g., CeFe contains 50 mol% Ce and 50 mol% Fe), except the SnFe whose tin and iron contents were 68 and 32 mol%. The ternary solids contents are 33 mol% for each metal (e.g., CeFeCo contains 33 mol% Ce, 33 mol% Fe and 33 mol% Co).

The XRD patterns of CeFe and SnFe nanocasted oxides possessed weak diffraction peaks (Fig. 1a) .

This result is in good agreement with those of previous studies, which indicated that the reflections of nanocasted oxides are broad and low in intensity [28–37]. Moreover, the XRD diffractograms suggested that the replicas of the oxides were more ordered than their template, which is common in amorphous materials. The reflection of CeFe and SnFe were related to cubic fluorite CeO_2 and tetragonal cassiterite SnO_2, respectively [16,20,28]. Alternatively, phases related to iron oxides were not detected; however, the size of iron oxide particles may be below the detection limit of XRD because SEM–EDX analyses indicated that iron oxides were present in CeFe and SnFe composites (Fig. 1b).

The peak intensities of MnFe composite were sharper than those of the CeFe and SnFe catalysts, indicating that metal oxide particles in CeFe and SnFe composites were smaller than those of MnFe. Indeed, the crystalline phase of MnFe contained Mn_2O_3 bixbyte, which was detected in higher amounts (68%) than in previous studies [1,16]. Although the Fe_2O_3 phase was relatively minor (22%), the presence of these phases cannot be neglected, as shown in the results of SEM–EDX analysis (Fig. 1b).

In addition, the crystallite size of the partially ordered MnFe composite was estimated from XRD peak at $2\theta = 38^\circ$ for Mn_2O_3 and the value was 17.0 nm. Also, for SnFe and CeFe crystallite sizes were calculated from XRD peak at about $2\theta = 30^\circ$ and the values were 21.5 and 28.4 nm, respectively.

XRD patterns of the ternary nanocasted oxides are shown in Fig. 1c. The results indicated that the primary phases of the CeFeCo catalyst were CeO_2 (36%), Co_2O_3 (42%) and spinel $CoFe_2O_4$ (21%). The CeFeZr composite consisted of 53.8% hematite Fe_2O_3 and 38.4% tetragonal ZrO_2. In case of CeFeNi, 36% of NiO and 64% of Fe_2O_3 were observed. Peaks related to crystalline CeO_2 were not detected in CeFeZr and CeFeNi, which indicates that crystalline CeO_2 was not present in the composites or was too small to be detected by XRD. Similarly, signals associated with CeO were not observed in the XRD patterns of Ce-based ternary oxides [20,28]. In CeNiAl, the primary phase consisted of spinel $NiAl_2O_4$, and NiO signals associated with $NiAl_2O_4$ were observed [12,13]. Cerium-based crystalline phases were not detected; however, SEM–EDX analysis indicated that cerium crystalline phases may be present in small amounts (Fig. 1d). Particles sizes of ternary composites were higher than that of the binary ones. The crystallite size of CeFeCo, CeFeZr, CeFeNi, and CeNiAl composites was 31, 64, 76, and 85 nm, respectively. They were estimated from the most intense peak of each sample.

Additionally, the ionic radii of Mn^{3+}, Sn^{4+}, Fe^{3+} are 0.64, 0.68 Å, 0.69 Å, respectively [8,38]; Ce^{4+} ion has the largest ionic radius of 0.94 Å, among the cations studied [38]. Hence, the presence of Sn^{4+} or Mn^{3+} could introduce cations in the Fe^{3+} framework; however, due to incomplete pore filling of the mold, isomorphoussly substituted binary composites were not observed; thus, monoxides of the elements are formed. In case of ternary oxides, the ionic radius of Co^{3+} (0.53 Å) enables this cation be randomly distributed in octahedral sites of the spinel structure, owing to the ionic radius proximity of Fe^{3+} (0.69 Å), as compared to those of Zr^{4+} (0.84 Å) and Ce^{4+} (0.94 Å) [38]. Al^{3+} possesses an ionic radius of 0.68 Å and will prob-

ably occupy a tetrahedral position in an almost inverse spinel with the Ni^{2+} (0.67 Å) ions preferentially distributed over the octahedral cation sites (A-site) in a AB_2O_4 binary spinel [12]. Accordingly, the spinel phases detected for CeNiAl and CeFeCo samples confirms the substitution of Ni^{2+} and Co^{3+} cations in octahedral sites of an Al_2O_4 and Fe_2O_4 matrices, respectively.

The variability of the crystalline phases may be caused by the conversion of the precursor salts in the pores of the template into inorganic nanoparticles during the thermal treatment. Moreover, the variability of the crystalline phases indicates that the mesostructure of the mold shrank during the impregnation step [16,29], and the narrow pores of the resin template led to the formation of nanoparticles on the exterior of the template.

Interestingly, in the XRD patterns of ternary composites, several higher angle peaks that were similar to that of the bulk oxides were observed. High angle peaks were attributed to the complete filling of the pores of the mold, resulting in the formation of the structural ordered oxides inside the pores, before its removal by calcination. In the case of binary solids, the amount of the metals precursors could be not enough to fill the pores of the template, resulting in a X-ray amorphous and/or nanocrystalline material. Another possible explanation lies in the fact that the spinel phases of the ternary solids are voluminous, while binary solids depict the lesser voluminous monoxides. The crystallinity could arise from the difference in filling of atoms inside and on the surface of the particle.

XAD-16 mold displays uniform spherical particles possessing diameters ranging from 100 Å to 200 Å. The particle morphologies of MnFe (Fig. 2a) and CeFe (Fig. 2b) composites were similar to that of the template. Previous studies [16,34] indicated that the solubility of iron nitrate is low compared to that of manganese. As a result, higher concentrations of iron nitrate were used, and the impregnations steps used to obtain rigid MnFe spheres were sufficient to break down the crystalline structure of Mn_2O_3 and Fe_2O_3 oxide spheres.

The results indicated that the resin beads must be washed to remove excess inorganic material from the surface of the bead and to separate agglomerated beads [28]. In addition, calcination in both air and nitrogen led to template carbonisation and the preservation of template morphology. As a result, after removal of the carbonised template, nanoparticle growth and connectivity was restricted to the pore volume. However, in SnFe composite (Fig. 2c), either iron or tin particles were formed outside of the mesoporous resin spheres, causing the spheres to agglomerate.

Interestingly, SEM image of SnFe composite revealed that the morphology was not similar to that of pure tin oxide or the resin, confirming that SnO_2 nanoparticles were not formed inside the pores of the resin due to cracking during the heating process. The replication of the morphology of SnFe composite was not confirmed by SEM analysis. The observed difference between the morphology of the mold and the referred oxide may not be interpreted as complete damage to the structural order. Sintering effects may have

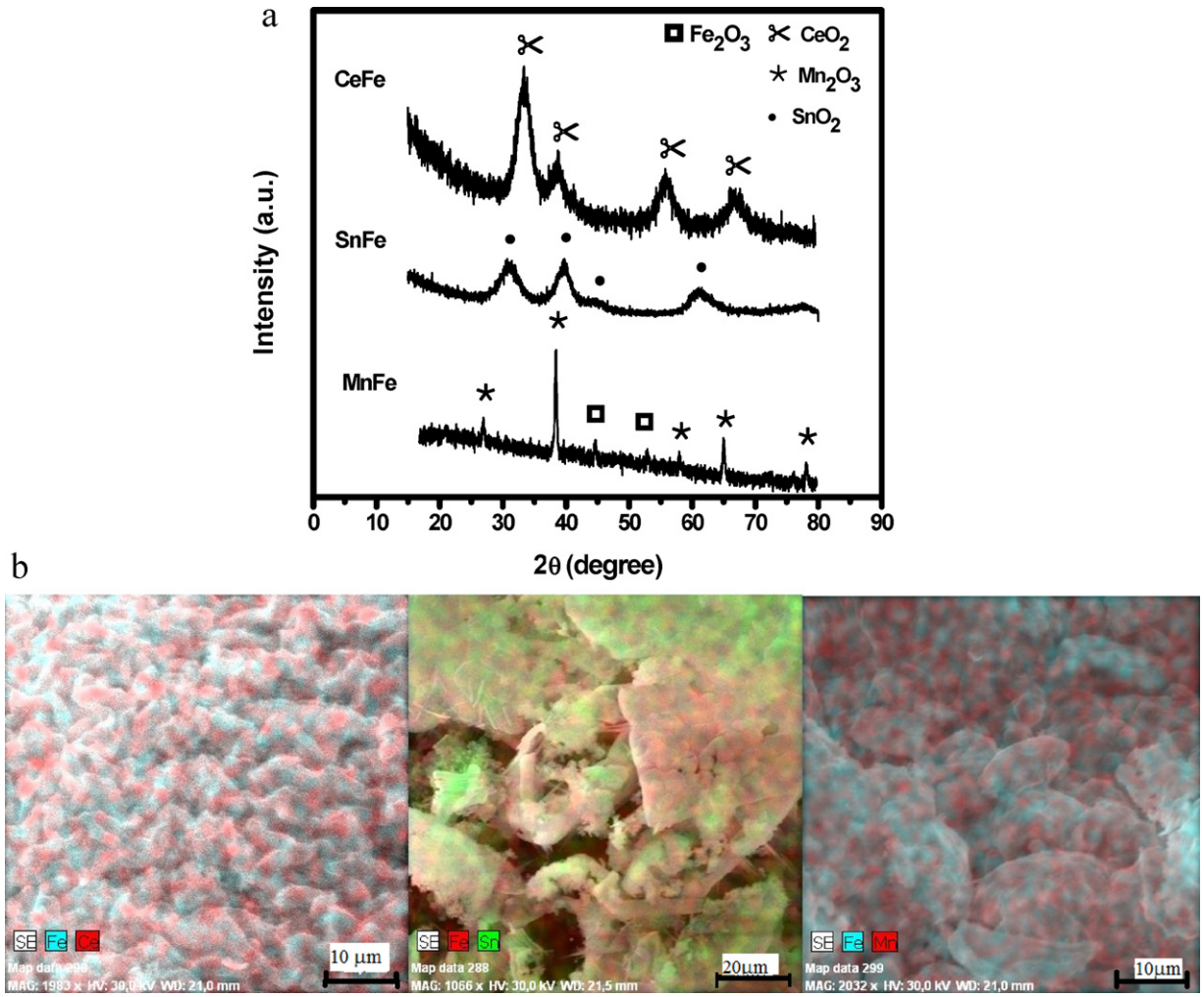

Fig. 1. (a) XRD patterns of the binary oxides. (b) SEM–EDX analyses of CeFe, SnFe and MnFe composites. (c) XRD patterns of the ternary oxides. (d) SEM–EDX analyses of CeFeZr, CeNiAl, CeFeCo and CeFeNi.

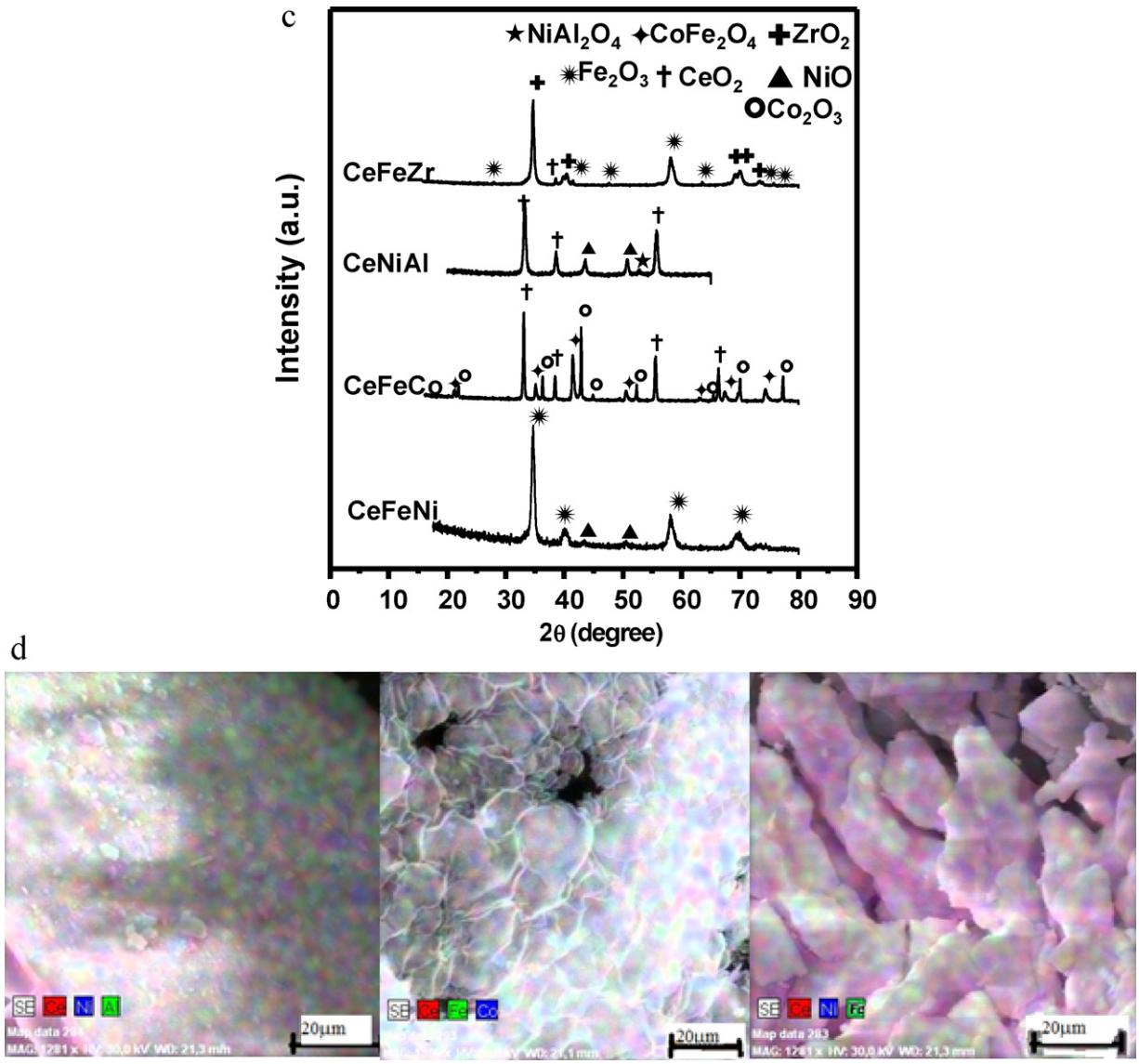

Fig. 1. *(Continued).*

caused a significant difference between the density of the open pores and that of the relative to that mold walls and oxide particles. Similar to the results of the present study, Smatt et al. [16] used a silica template and high concentrations of $SnCl_2$ to obtain SnO_2 aggregated nanocrystalline particles.

The morphology of the ternary composites consisted of aggregated spheres. In CeNiAl, the morphology of the internal region of the spheres was uniform, and uneven shrinkage or deformation was not observed (Fig. 2d). Moreover, the morphology of CeFeCo was nearly spherical (Fig. 2e), and a fraction of the particles in the CeFeCo composites possessed circular craters, which may have originated from replication at contact points between the mold during the inorganic precursor decomposition, as observed in early works [16,21]. Fig. 2f and g showed the surface of CeFeZr and CeFeNi composites was rough, and loosely packed particle aggregates between 15 and 200 Å were observed. Upon impregnation, the solidity of the spheres increased; however, the overall mechanical stabilities of CeFeZr and CeFeNi spheres were quite low due to the formation of bulk phases, as confirmed by XRD analysis. Nitrogen adsorption–desorption isotherms of the samples, as well as the pore size distribution, are shown in Fig. 3.

During the filling step, the relative pressure of the XAD-16 mold ranged (P/P_o) from 0.2 to 0.8 due to the filling of framework-confined mesopores (Fig. 3a). In addition, the BET surface area of the mold was 800 $m^2\,g^{-1}$, and the pore volume was 1.82 $cm^3\,g^{-1}$. Indeed, the pore diameter of the template was in the 15–20 nm range, confirming that the porous characteristics of the resin could be attributed to type IV isotherm. Moreover, due to the intra-particulate porosity and the ability to simultaneously tune the chemical composition of the spheres and the particle size, the proposed replica structures are highly accessible, and diffusion into the template pore during the impregnation of the metals is unlimited [28,34]. Consequently, the solids have high textural properties compared to those obtained by co-precipitation and sol-gel methods [34–43].

The MnFe binary composite adsorbed N_2 at relative pressures (P/P_o) greater than 0.7 (Fig. 3b) due to the presence of non-framework mesopores or interparticle voids, which is a typical characteristic of mesoporous transitional-metal oxides replicated via nanocasting [13,15–20,30–34]. Both SnFe and CeFe samples showed N_2 adsorption–desorption isotherms characterised by mesoporous metal oxides prepared by hard template route with a small step and an H1-type hysteresis loop at P/P_o 0.2–0.4 [15,22].

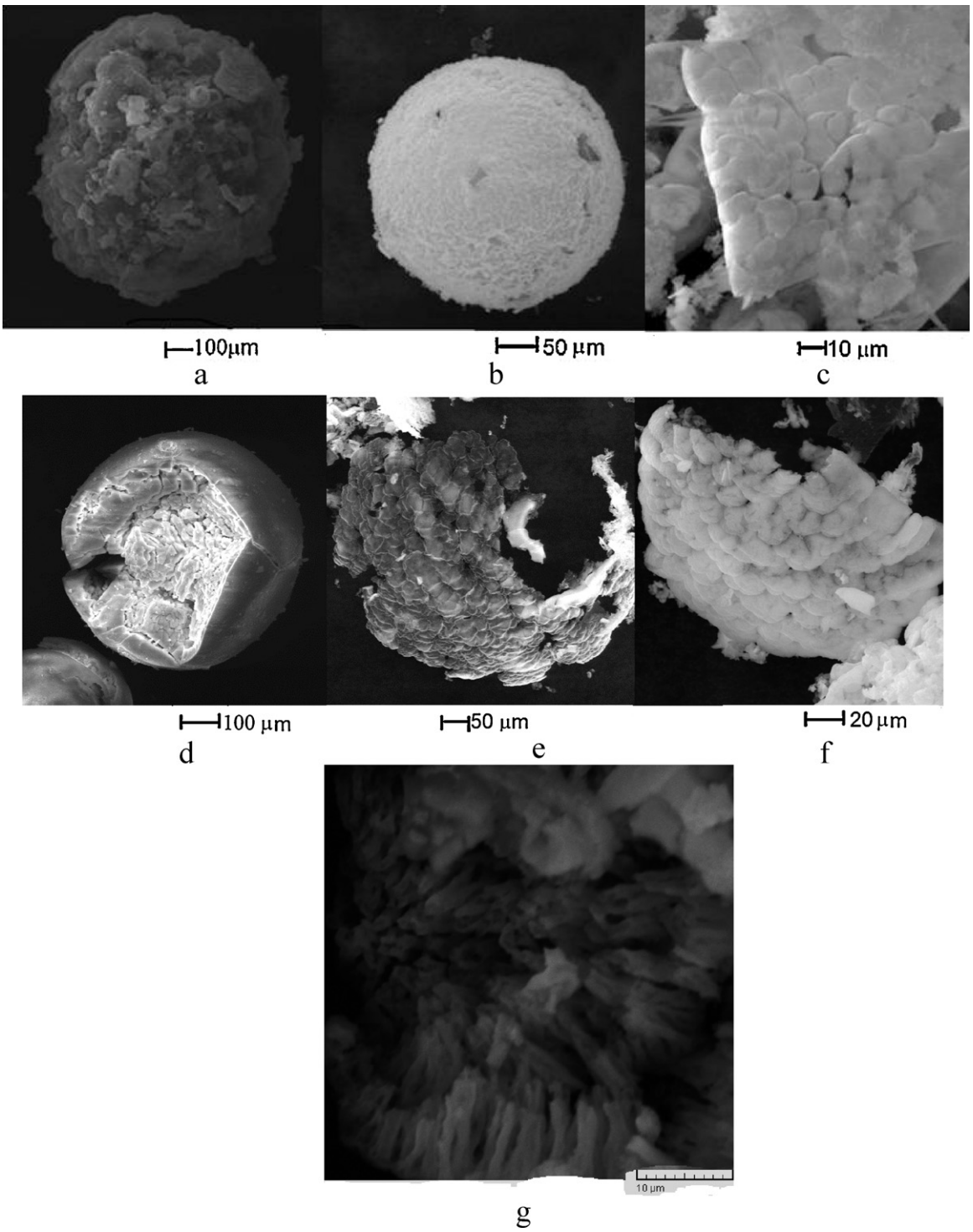

Fig. 2. SEM images of the nanocomposite oxides: (a) MnFe (b) CeFe, (c) SnFe, (d) CeNiAl, (e) CeFeCo, (f) CeFeZr and (g) CeFeNi.

Except for CeNiAl, the ternary composites showed typical type IV isotherm with hysteresis loops, which indicated the formation of a mesostructure (Fig. 3b).

The pore structures of all these materials revealed that all of them had a uniform pore size distribution (Fig. 3c), and the final oxides had pore diameters below to 15 nm. Thus, the mesostructure of the mold has been partially preserved after its impregnation with the metals, except for CeNiAl. Accordingly, the BET surface areas, BJH pore sizes and corresponding pore volumes of the oxides are listed in Table 1.

All the mesoporous oxides replicas exhibit relatively large BET specific surface areas (>51 $m^2\ g^{-1}$). This means that the oxides synthesised by nanocasting replication method have the merits of well-maintained large surface areas and pore volumes as well as homogeneous dispersion of components.

Compared to the values of the resin template, it could be found that all the binary composites have surface area in the range of 115–374 $m^2\ g^{-1}$ and pore volume in the range of 0.34–1.10 $cm^3\ g^{-1}$. The findings points out that the high porosity of the template is well reflected in the final oxide, however, growth of the inorganic

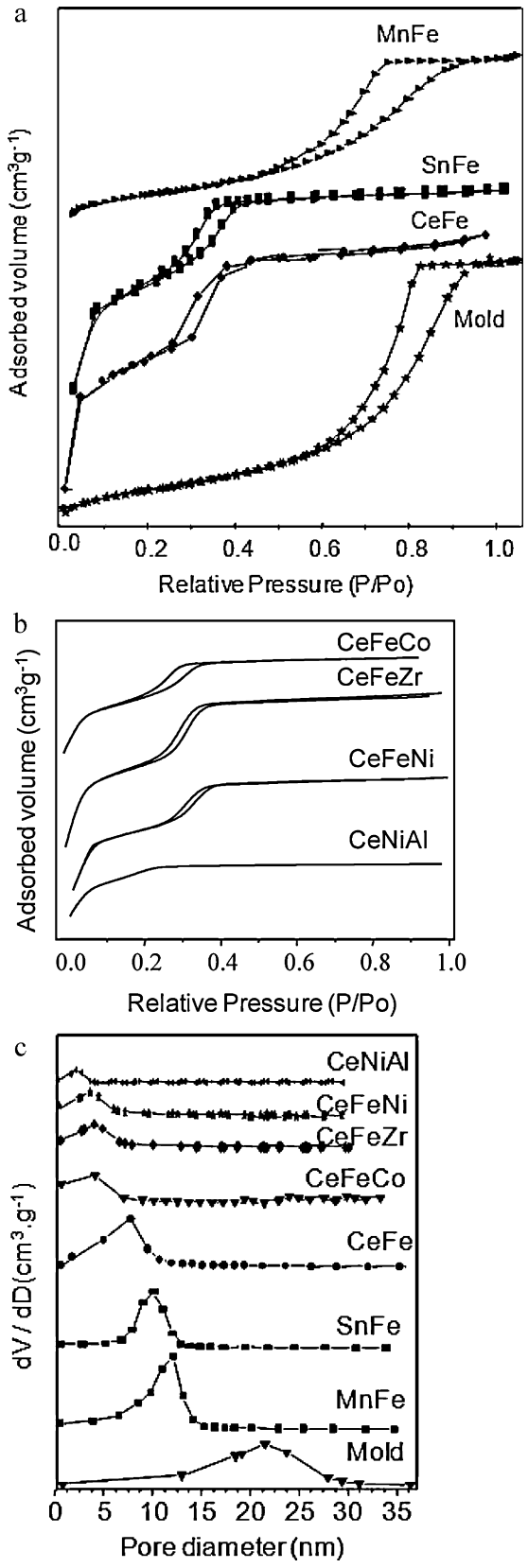

Fig. 3. Nitrogen adsorption–desorption isotherms measurements: (a) binary composites and (b) ternary composites. (c) The pore size distribution of the solids studied.

Table 1
Textural properties of the solids.

Sample	Sg[a] ($m^2\,g^{-1}$)	Vp[b] ($cm^3\,g^{-1}$)	Dp[c] (nm)
MnFe	374	1.10	10.8
SnFe	140	0.41	7.0
CeFe	115	0.34	6.8
CeFeCo	92	0.24	5.2
CeFeZr	85	0.20	4.6
CeNiAl	74	0.17	4.0
CeFeNi	51	0.14	3.2

[a] From BET method.
[b] From the adsorption branch at $P/P_o = 0.99$.
[c] From desorption branch using BJH method.

crystallites, sintering and shrinkage effects during calcination prevent that the final oxide represents an exact replica of the template structure, as found in the findings [18,34–37].

Indeed, during the thermal treatment, the salt precursors diffuse into the inner regions of the spheres before nucleation and growth of the nanoparticles can occur. As a result, larger pores could be observed in the interior of the particles, compared to pores close to the surface. However, the ternary composites possessed lower surface areas (e.g., 51–92 $m^2\,g^{-1}$) and pore volumes (e.g., 0.14–0.27 $cm^3\,g^{-1}$) than their binary counterparts, which can be attributed to the wall thickness of the resin template (about 5 nm), as shown in Table 1.

The results of previous studies [16,20,37] indicated that the structure of the oxides develops during impregnation/precursor decomposition. However, when a third metal infiltrates into the pores of the mold, the restricted access of the template provoke the formation of the oxides inside the pore mold. CeFeNi presented the lowest textural properties due to the agglomeration of bulk phases on the mold surface, as evidenced in SEM and XRD analyses.

The resin exhibited a narrow pore size distribution. Nevertheless, the structure of the mold was well replicated in some oxides. Changes in the internal structure of the replicas resulted in differences in the pore size distribution, revealing that an increase in the microporosity of the solids could be achieved.

3.1.1. TPR analyses

Fig. 4 shows the TPR profiles of the catalysts.

As shown in Fig. 4a, three peaks centred at 330 °C, 465 °C and 515 °C were observed in the TPR profile of MnFe. Indeed, the TPR profile exhibited features between 760 and 840 °C. The lower temperature peaks were assigned to the reduction of Fe_2O_3 to Fe_3O_4 and the reduction of Fe_3O_4 to FeO and its further reduction to Fe^0 [3,11,39], respectively. Free iron nanoparticles (not detected by XRD) were easily reduced at relatively 330–515 °C temperatures due to their exposure on the surface of the mold, according to the findings [39]. The shoulder at about 550 °C could be assigned to the pore occluded iron particles. The higher temperature peaks (e.g., 760–840 °C) were assigned to the reduction of bulk Mn_2O_3 to MnO_2 and the reduction of MnO_2 to Mn^0 [21,40]. Mn_2O_3 and MnO_2 were reduced at high temperatures due to the low accessibility of these species to hydrogen. The small oxide crystallites may be present within the composite due to the high surface area and the low reducibility of Mn_2O_3 (Table 1). The results indicated that the reduction of Mn_2O_3 was almost complete in the MnFe catalyst. Moreover, free Fe_2O_3 was probably present on the surface of the solid and the catalyst was composed primarily of Mn_2O_3; thus, isolated phases of mixed oxides were present within the material.

In the TPR profile of CeFe, a board peak at 510–760 °C. Similar to MnFe, the low temperature peaks were assigned to the two step reduction of iron at 600 °C and 710 °C. Although MnFe and CeFe catalysts displayed similar profiles of reduction temperatures, the CeFe catalyst exhibited unique features in the H_2-TPR profile

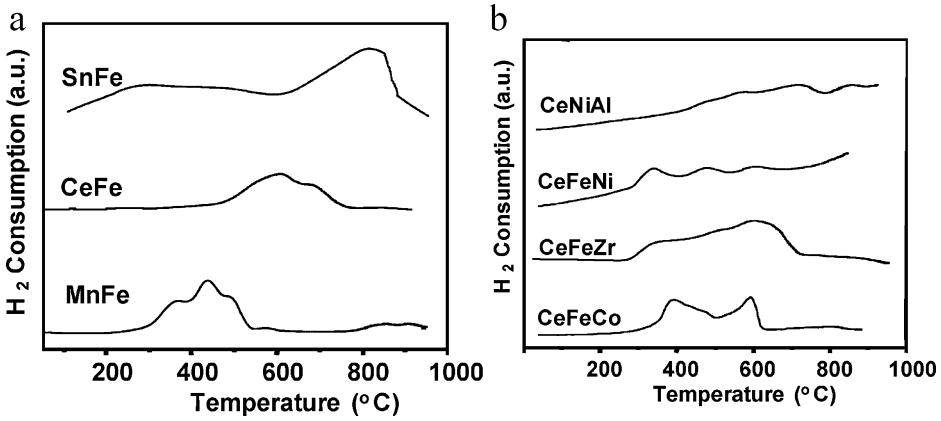

Fig. 4. TPR analyses of the composites: (a) binary oxides and (b) ternary oxides.

and the Fe^0 peak was significantly diminished. The broad peak at 510–760 °C in the TPR profile of CeFe was associated with the reduction of CeO_2 on the solid surface. Indeed, this peak may be associated with the bulk reduction of CeO_2 [41,42] via the formation of oxygen vacancies in the structure of fluorite and subsequent dissociation of H_2O to form bridging OH groups or the direct dissociation and transport of H_2 to the ceria surface [43,44].

The TPR curve of SnFe catalysts displayed reduction peaks between 220 and 550 °C and 600 and 800 °C. The first peak was associated with the reduction of amorphous iron, as evidenced by XRD and SEM–EDX measurements. Alternatively, the second peak was related to the reduction of Sn^{4+}/Sn^3 to Sn^{2+} and the reduction of Sn^{2+} to Sn^0, which is in line with earlier observations for SnO_2/Fe_2O_3 nanocomposites [45,46]. Indeed, the amount of hydrogen consumed by the latter process was significantly higher than that of the former, which is characteristic of SnO_2.

The CeFeZr catalyst (Fig. 4b) exhibited a profile that was similar to that of CeFe. As expected, peaks related to the reduction of ZrO_2 were not observed. The CeO_2 reduction peaks shifted to slightly higher temperatures due to the presence of Zr, which prevented CeO_2 reduction whereas that of Fe_2O_3 was shifted to lower temperatures Also, the introduction of Zr changed the shape of the TPR profile, and the mobility of oxygen at the surface altered the oxidation states of surface Fe^{3+} and Ce^{4+}/Ce^{3+} ions, probably.

On the contrary, the CeFeCo catalyst showed a broad reduction peak between 340 and 600 °C, indicating that the reduction of Fe_2O_3, Co_2O_3 and CeO_2 occurred simultaneously. Thus, the redox ability of the phases was improved due to electron transfer from CeO_2 to Fe_2O_3 and Co_2O_3 [21,46,47]. Electron transfer between metal oxides was evidenced in the hydrogen consumption peaks of CeFeCo. Specifically, the low temperature peak was attributed to the reduction of surface capping oxygen species (O^{2-} or O^- anions) and/or the stepwise reduction of ceria by the elimination of O^{2-} anions from the lattice due to the formation of Ce_2O_3 (cerium redox couples Ce^{4+}/Ce^{3+}) [21,43], which increases as the amount of Co_2O_3 and Fe_2O_3 within the material increases. Although spinel $CoFe_2O_4$ is reduced at temperatures greater than 600 °C [46], this process was not observed in the present study due to the high heating rates employed during the analysis.

Additionally, the CeNiAl catalyst showed a large peak at 410–920 °C. The higher temperature peak of the TPR profile of CeNiAl was narrow, suggesting that the crystalline domain increased due to the aggregation of Ni^{2+} nanocrystallites inside the mold, which is difficult to reduce. Furthermore, the presence of amorphous Ce may suppress nickel reduction. The peaks in the TPR profile of CeNiAl at temperatures greater than 800 °C were associated with $NiAl_2O_4$ reduction [8,12].

The TPR profile of CeFeNi was similar to that of CeNiAl. Nevertheless, peaks associated with Ni^{2+} were shifted to lower temperatures because unstable Ni^{3+} species are highly reducible and can promote the reduction of Ni^{2+} to Ni^0 [12]. Moreover, the measurements suggested that Ni^{2+} can interact freely with the mold causing an increase in the surface energy of NiO, which is not stabilised by Fe_2O_3 nanocrystallites. At high temperatures (>800 °C), a peak related to the reduction of Fe_2O_3 was observed; thus, CeO_2 may be able to interact with Fe_2O_3.

3.1.2. CO_2-TPD measurements

The CO_2-TPD curves of the catalysts are shown in Fig. 5.

The CO_2-TPD profiles of CeFe and MnFe composites displayed interesting features (Fig. 5a). The onset of CO_2 desorption on mesoporous CeFe began at approximately 457 °C, and maximum oxygen desorption was obtained at 580 °C. The location of the aforementioned peaks indicated that medium and high strength basic sites were present in the material. However, the results suggested that the number of basic sites in the composite was relatively low. Because of the smaller size and lower charge density of Fe^{3+}, the addition of Fe_2O_3 nanoparticles caused the CeO_2 lattice to contract. Moreover, oxygen vacancies in the lattice were generated to overcome the resultant charge imbalance, enhancing lattice contraction. A similar effect has been observed in the CO_2-TPD data of CeO_2–Fe_2O_3 [48]. In MnFe nanocomposites, two low intensity oxygen desorption bands were observed at 250 and 400 °C due to the mild acidity of Mn_2O_3. Interestingly, the intensity of the peak at 600 °C suggested that the addition of Fe_2O_3 nanocrystallites increased the number and strength of basic sites present in the material. The CO_2 desorption profile of SnFe was nearly a straight line due to the acidity of Sn and Fe species. Moreover, basicity of the binary oxides was high over CeMn and MnFe while SnFe an acidic sample.

The CO_2-TPD profiles of the CeFeZr and CeNiAl mixed oxides contained a triple desorption peak at a maximum temperature of 100–300 °C while CeFeNi and CeFeCo displayed one peak. The triple desorption peak of the CeFeZr and CeNiAl oxides spanned from 100 °C to 600 °C (Fig. 5b).

CeFeCo exhibited a small peak at 610–800 °C and a sharp high temperature reduction peak at 580 °C, similar to that of CeFe. The low temperature peak suggested that lattice contraction occurred, and the high temperature peak indicated that CeFeCo mixed oxide was quite basic. Thus, CeFeCo composites possessed strongly basic sites due to the formation of $CoFe_2O_4$ and Co_2O_3.

In the CO_2-TPD profile of CeFeZr, three desorption peaks centred at 200, 304,510 and 700 °C were observed. The low intensities peaks were related to the presence of mild and medium strength basic sites. Nevertheless, at high temperatures, a relatively intense peak

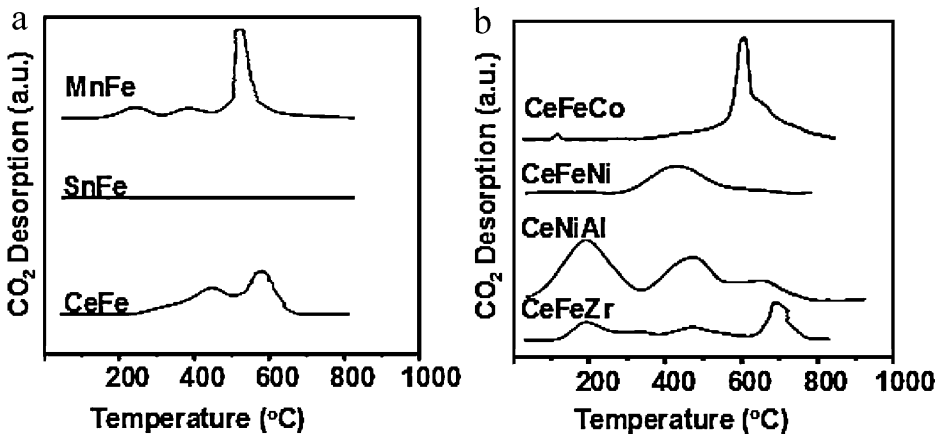

Fig. 5. CO_2-TPD analyses of the composites: (a) binary oxides and (b) ternary oxides.

characteristic of high strength basic sites was observed, ZrO_2 can interact with Fe_2O_3 and CeO_2, and declines the basicity of the solid but this was not observed over CeFeZr.

The CO_2-TPD profile of CeFeNi displayed only one peak between 400 and 600 °C, which was assigned to basic sites of high strength. Compared to CeO_2, NiO and Fe_2O_3 phases were the most acidic sites in the catalyst. Additionally, a strong synergetic effect between NiO and Fe_2O_3 phases was observed, and the crystallisation of the CeO_2 phase was limited. Although CeO_2 exists as separate crystallites in the mesoporous composites, the presence of CeO_2 increases the basicity of the material due to its ability to store oxygen.

Interestingly, the TPD profile of CeNiAl exhibited two broad and well defined reduction peaks at 200 and 500 °C, and another weak and broad peak at approximately 680 °C. The intensity of the peaks was attributed to the dispersion of NiO throughout the $NiAl_2O_4$ phase [8], which was formed by solid-state reactions. The existence of an amorphous CeO_2 phase increased the basicity of the material and the dispersion of NiO, probably. The TPD peaks obtained in the present study were not well resolved; thus, the data was not quantified.

Hence, difference in basic strength of the ternary oxides must truly be caused by the presence of Zr, Ni, and Fe species that modified the oxidation state of the surface CeO_2, by generating a spread of strengths for the basic sites. This is the reason for what mild, medium and strong strength basic sites are formed on CeFeZr, CeNiAl whereas CeFeNi possessed only medium strength basic sites. CeFeCo possessed basic sites of strong strength due to the formation of $CoFe_2O_4$ and Co_2O_3, as aforesaid.

3.2. Catalytic measurements

The activity of the materials in the dehydrogenation of ethylbenzene in the presence of CO_2 at 550 °C, and CO_2/EB = 30 was determined. The results are shown in Figs. 6 and 7.

Control tests using the same feed and an empty or filled quartz reactor yielded 0% CO_2 conversion and <0.1% ethylbenzene conversion, respectively. The XAD-16 template was inactive to the dehydrogenation of EB.

Over time, the activity of SnFe decreased until a constant conversion of ethylbenzene was obtained, and then decreased after approximately 400 min on stream. MnFe possessed a lower activity level than SnFe throughout the reaction, whereas CeFe deactivated slowly and displayed a steady state EB conversion of 4%. The results indicated that iron nanoparticles (evidenced by SEM–EDX measurements), which are responsible for the dehydrogenation of ethylbenzene [6,11,13], are reduced to form large oxides due to the presence of hydrogen gas at high temperatures. As a result, a layer

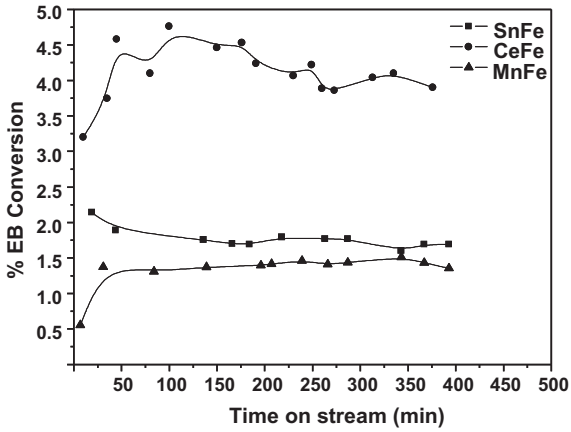

Fig. 6. Conversion of ethylbenzene as a function of time on stream for binary oxide composites. Reaction conditions: catalyst: 50 mg; N_2: 11.7 mmol h^{-1}; CO_2: 58 mmol h^{-1}; EB: 1.98 mmol h^{-1} (CO_2/EB ratio = 30); T = 550 °C.

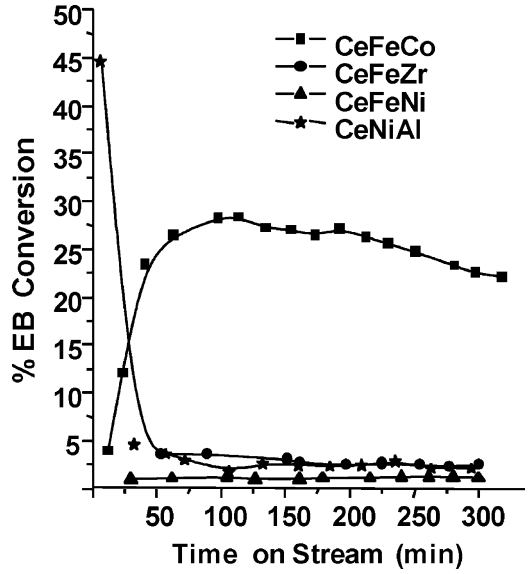

Fig. 7. Conversion of ethylbenzene as a function of time on stream for ternary oxide composites. Reaction conditions: catalyst: 50 mg; N_2: 11.7 mmol h^{-1}; CO_2: 58 mmol h^{-1}; EB: 1.98 mmol h^{-1} (CO_2/EB ratio = 30); T = 550 °C.

Table 2
Products distribution for binary and ternary oxides composites. Reaction conditions – catalyst: 50 mg; N_2: 11.7 mmol h^{-1}; CO_2: 58 mmol h^{-1}; EB: 1.98 mmol h^{-1} (CO_2/EB ratio = 30); T = 550 °C. Others products included methane, ethane, carbon monoxide, water and polyaromatics.

Sample	% products distribution			
	Styrene	Benzene	Toluene	Others products
MnFe	35.0	24.1	5.0	36.0
SnFe	10.5	19.6	23.3	46.3
CeFe	58.0	12.0	15.0	15.0
CeFeCo	56.0	17.2	13.8	13.0
CeFeZr	27.0	21.5	17.8	34.0
CeNiAl	19.6	12.5	46.9	20.9
CeFeNi	9.2	34.3	27.0	29.4

of sintered particles and carbon were simultaneously deposited on the surface of the CeFe catalyst (Fig. 3i).

Neither the low reducibility of SnO_2 nor the high surface area of the sample impeded the modest performance of SnFe, as revealed by the TPR results and the textural properties of the material. The activity of the composite was increased due to the ability of Sn to suppress iron reduction (TPR results), which is in good agreement with earlier observations for SnO_2/Fe_2O_3 nanocomposites [45]. However, nanocasted SnO_2 was nearly inactive, and the conversion of EB was attributed to iron nanoparticles. MnFe possessed a high surface area (Table 1); however, the performance of the catalyst was less than that of SnFe due to the presence of highly reducible Mn^{2+} species (Mn_2O_3). The redox ability of Mn_2O_3 in MnFe oxide catalyst is improved due to electron transfer from the Fe_2O_3 oxide phase, which is significantly enhanced in nanocasted manganese oxide materials [21]; however, this effect was not observed in the present study.

As shown in Fig. 6, the highest activity among the binary composites was obtained with CeFe, indicating that CeO_2 and Fe_2O_3 have a synergistic effect on EB dehydrogenation. Thus, the results suggested that the reducibility, basicity and textural properties of the materials had an effect on ethylbenzene dehydrogenation. Moreover, the effects of ceria oxide are well established in the literature [1,21,42]. Due to the high reactivity of mesoporous ceria in a reducing media, partially reduced ceria, $CeO_{2-\delta}$, can donate electrons to Fe_2O_3 oxide in the RGWS reaction (reaction (I)). Thus, the presence of CO_2 produces redox couples (Fe^{3+}/Fe^{2+}) [6,8,11], which can further promote the reduction of CeO_2 and the oxidation of iron.

$$CO_2 + H_2O \rightarrow H_2 + CO \quad \text{(I)}$$

However, this effect is rather limited and reduces the activity of ethylbenzene dehydrogenation.

As shown in Table 2, CeFe was highly selective for the production of styrene, and a change in the distribution of products was not observed for CeFeCo, indicating that the ability of mesoporous CeO_2 and Fe_2O_3 oxides to catalyse oxidative EB dehydrogenation is excellent. Byproducts such as toluene and benzene were formed in a lesser amount. Others products included methane, ethane, and polyaromatics are observed. The amounts of these products were high over SnFe, MnFe, CeFeZr, CeNiAl and CeFeNi catalysts. Indeed, theses solids were less selective to styrene. This type of peculiar character of mixed oxides has already been reported for the dehydrogenation of ethylbenzene and were a result of thermal cracking and condensation reactions occurred as expense of the ethylbenzene dehydrogenation [8,13,52].

Fig. 7 displays the initial conversion and stability of the ternary catalysts over time on stream. The results indicated that the catalytic conversion and selectivity to styrene for CeFeZr and CeFeNi were less than 3% and 20%, respectively, because CeFeZr and CeFeNi are easily reduced in the reaction media, as demonstrated by TPR analyses. Indeed, the presence of ZrO_2 did not provide additional stability in CeFeZr, and the harsh environment of the reaction facilitated the phase transition of zirconium.

The textural properties of the catalyst were low, which suggests that the accessibility of reactants (EB, CO_2) to iron, nickel, and cerium actives sites is limited. Indeed, basic sites of high strength in CeFeZr did not enhance the catalytic performance of the solid due to the lack of occurrence of the following reaction:

$$Ø\text{-}CH_2CH_3 + CO_2 \rightarrow CO + H_2O + Ø\text{-}CH{=}CH_2 \quad \text{(II)}$$

Reaction (II) is initiated by the high adsorption capacity of CO_2 and the basicity of ceria [39]. Because basic sites have a lower adsorption capacity, the production of styrene via reaction (II) is difficult over CeFeZr. In contrast, the catalytic activity of CeNiAl was initially high and decreased to a steady state conversion of 5%. The conversions within 50 min on stream (Fig. 7) were compared, and the results revealed that CeNiAl was the most active catalyst. The relatively high activity of CeNiAl may be attributed to the large number basic sites of medium strength from amorphous CeO_2 and a highly active spinel $NiO/NiAl_2O_4$ phase [12,13,49]. The aforementioned basic sites catalyse CO_2 conversion and the spinel phase catalyses EB dehydrogenation; thus, the activity of CeNiAl decreased as the latter phase was consumed. This result is in agreement with the general belief that moderately basic sites and a large stable phase can catalyse the dehydrogenation of EB at low temperatures.

Moreover, the basic sites of $CoFe_2O_4$, which corresponded to CO_2-TPD desorption at 600–800 °C, played a significant role in EB dehydrogenation, providing further evidence that the spinel phase is the most active site in EB dehydrogenation. The equilibrium conversion of EB and the selectivity for styrene production of CeFeCo under the applied conditions were 25% and 80%, respectively. In CeFeCo, the presence of Fe_2O_3, Co_2O_3 and the basic sites of CeO_2 increased EB conversion due to the reduction of CeO_2 surface capping oxygen species, as evidenced in the TPR results. On the contrary, CeFeCo displayed a broad reduction peak at lower temperatures, which suggested that Fe_2O_3, Co_2O_3 and CeO_2 were reduced simultaneously. The reduction of spinel $CoFe_2O_4$ was superior at 600 °C; thus, the basic sites of medium strength and the spinel phase of CeFeCo provided the highest catalytic performance.

The highest activity was observed with CeFeCo, followed by CeFe, MnFe and CeFeZr; however, MnFe displayed the highest textural property values, followed by CeFe, CeFeCo and CeFeZr. These results indicate that a redox reaction occurs over CeFeCo during the dehydrogenation of EB, which is in accordance with previous results [13]. The presence of redox reactions indicates that the accessibility of the reactants to the active sites is dependent on the size of the exposed area and the porosity of the solids. Additionally, the conversion of ethylbenzene and CO_2 were compared, and the results revealed that ethylbenzene conversion was higher than carbon oxide conversion for all of the catalysts due to the presence of the following side reactions (reactions (III)–(VI)):

$$Ø\text{-}CH_2CH_3 \rightarrow Ø + C_2H_5 \quad \text{(III)}$$

$$Ø\text{-}CH_2CH_3 \rightarrow Ø\text{-}CH_2 + CH_4 \quad \text{(IV)}$$

$$Ø\text{-}CH_2CH_3 \rightarrow C + 5H_2 \quad \text{(V)}$$

$$2Ø\text{-}CH{=}CH_2 \rightarrow \text{coke} + 6H_2 \quad \text{(VI)}$$

A reverse water shift reaction consumes CO_2, and results in the formation of coke:

$$CO_2 + 2H_2 \rightarrow C + 2H_2O \quad \text{(VII)}$$

$$CO + H_2 \rightarrow C + H_2O \quad \text{(VIII)}$$

The product distribution of the catalysts revealed that styrene was the main product of iron-based catalysts, and the minimum

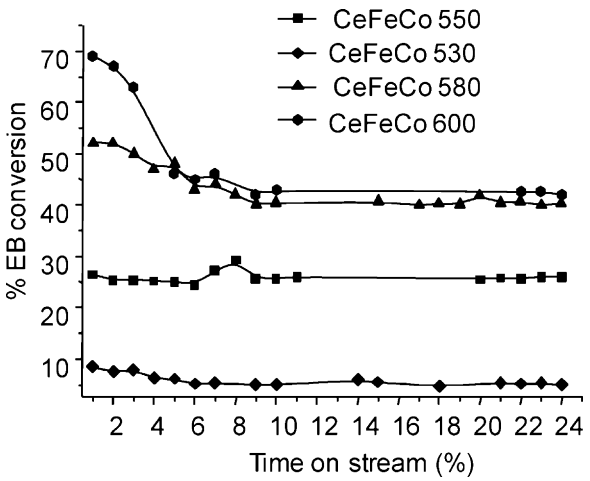

Fig. 8. Conversion of ethylbenzene as a function of time on stream for ternary CeFeCo oxide. Reaction conditions: catalyst: 50 mg; N_2: 11.7 mmol h^{-1}; CO_2: 58 mmol h^{-1}; EB: 1.98 mmol h^{-1} (CO_2/EB ratio = 30); T = 530–600 °C.

selectivity of the catalysts was 30% (Table 2). Moreover, the selectivity of the catalysts decreased with an increase in conversion. As shown in Table 2, the selectivity for styrene production followed the same trend as ethylbenzene conversion. Moreover, at 25% conversion, a significant amount of toluene and benzene, which are produced via reactions (III) and (IV) respectively, were observed. A number of unknown byproducts were also observed; however, the presence of cracked product was not detected. Heavier products derived from ethylbenzene or styrene oligomerisation appeared in the dehydrogenation of EB by CeFeNi and CeNiAl, which suggested that high molecular weight products resulted from the oligomerisation of styrene over Ni active sites rather than Fe sites. These results are in accordance with those of other studies, which demonstrated that heavy aromatic products result primarily from styrene oligomerisation on Ni sites, and that iron sites were selective for styrene production [8,11,12,13].

Therefore, the low activity of the binary oxides was caused by the reduction of the active phase and sintering effects. Furthermore, it is worth noticing that, for CeFeCo catalyst after reaction, there is a considerable difference in carbon formation and quality.

3.2.1. *Effect of reaction temperature on the catalytic activity and stability*

The catalytic performance of CeFeCo at different reaction temperatures is presented in Fig. 8. Results for the steady state condition are summarized in Table 3.

The conversion of EB increased with an increase in the reaction temperature. At low temperatures (<530 °C), the amount of heat supplied to the reaction was insufficient for EB dehydrogenation, and approximately 5% conversion was obtained at equilibrium. Styrene was the predominant product at low conversion over iron-based catalysts, indicating that styrene is the primary product of iron-catalysed EB dehydrogenation. The majority of the studies on the effect of temperature on ethylbenzene conversion indicate that an increase in temperature improves EB conversion and decreases the selectivity for styrene production because cracking predominates at higher temperatures [6–8,11,12,13]. Similarly, in the present study, the selectivity to styrene decreased at temperatures greater than 530 °C (Table 3) because ethylbenzene began to crack, resulting in the formation of toluene, benzene or coke. The results indicated that the catalyst did not display favourable activity at temperature as low as 530 °C after 24 h on stream.

Table 3
Catalytic performance of the CeFeCo solid obtained at different temperatures. Reaction time: 24 h.

Sample	% conversion	% selectivity to styrene	Activity (mmol g^{-1} h^{-1})
CeFeCo 530	5.0	50.0	4.5
CeFeCo 550	25.9	45.0	37.6
CeFeCo 580	40.0	23.3	115.8
CeFeCo 600	42.0	22.0	121.2

At higher temperatures (e.g., 550 °C), a sharp increase in activity was observed; however, the catalyst deactivation during a much longer time was due to reduction by CO or H_2, and the formation of coke (as depicted further in Fig. 9). Coke was not removed by the RGWS reaction, and the activity of the catalysts was not enhanced as the temperature increased from 580 to 600 °C. Moreover, the highest catalytic activity was observed in the first hours of the reaction during the induction period for ethylbenzene dehydrogenation at 600 °C (Fig. 8). After the induction period, coking on the solid surface was observed, and ethylbenzene dehydrogenation became thermodynamically forbidden due to the predominance of side reactions (VI) and (VII) at 580–600 °C [6,11,49–54].

When the reaction temperature is greater than 580 °C, the effects of the side reactions on the kinetics of the reaction can be neglected. However, the equilibrium conversion of ethylbenzene was 45% at 600 °C and subsequently decreased to 42% in the steady state. However, the conversion of EB could be controlled at 5–25% by tuning the contact times [6,52–55]. The steady state conversions of EB were significantly lower than the corresponding thermodynamic equilibrium conversions, which reached 40–98% [6,52]. Therefore, the temperature of the reaction was maintained below 550 °C to control the kinetics of EB dehydrogenation.

In addition, the total flow rate was controlled 60 mL min^{-1} to eliminate external diffusion resistance. EB conversion was accompanied by carbon deposition (reactions (V)–(VII)), which may lead to the deactivation of the catalyst. Therefore, the activity of the CeFeCo catalyst was too low at 530 °C and greatly increased to 115.8 mmol g^{-1} h^{-1} at 580 °C (Table 3). However, activity experienced a slightly increase (e.g., 121.2 mmol g^{-1} h^{-1}) at 600 °C after 24 h on stream. Carbon deposition caused the slightly decrease in the activity. The mechanism of the EB dehydrogenation may vary below 530 °C; however, the mechanism remains constant at temperatures greater than 600 °C. Thus, the conversion of EB can be divided into three regions, 530 °C, 550 °C and up to 580 °C, and the mechanism of the reaction is constant at low and high temperatures, and varied at moderate temperatures.

Moreover, with CeFeCo catalyst, the conversion and the selectivity to styrene reached 40 and 22%, respectively (Table 3). These results are lower than that of the current industrial process using Fe–Cr–K operated at a temperature as high as 600–700 °C, in the presence of a large amount of superheated steam [54,55]. However, the commercial Fe–Cr–K catalysts do not work effectively in the alternative dehydrogenation of ethylbenzene by CO_2 (ODH) process [55]. Therefore, the ODH over CeFeCo nanocasted oxide could be an alternative to produce styrene due to its increased stability at 550–580 °C temperature range. Due to the use of high temperatures in the dehydrogenation process, iron based catalysts quickly deactivate due to sintering of the active metal phase and coke deposition, however, the structural, textural and morphological properties of the nanocasted CeFeCo improved considerably its catalytic performance in the ODH reaction.

3.3. *Raman, FTIR and SEM analyses of spent catalysts*

Fig. 9a shows the FTIR spectra of CeFeNi, CeFeCo and CeNiAl. The bands at 3200–3600 cm^{-1} were attributed to the stretching vibration of the OH group from H_2O generated during the reaction. The shoulders around 1557–1650 cm^{-1} corresponded to asymmetric and symmetric C=C and C–C stretching modes [12] of heavy aro-

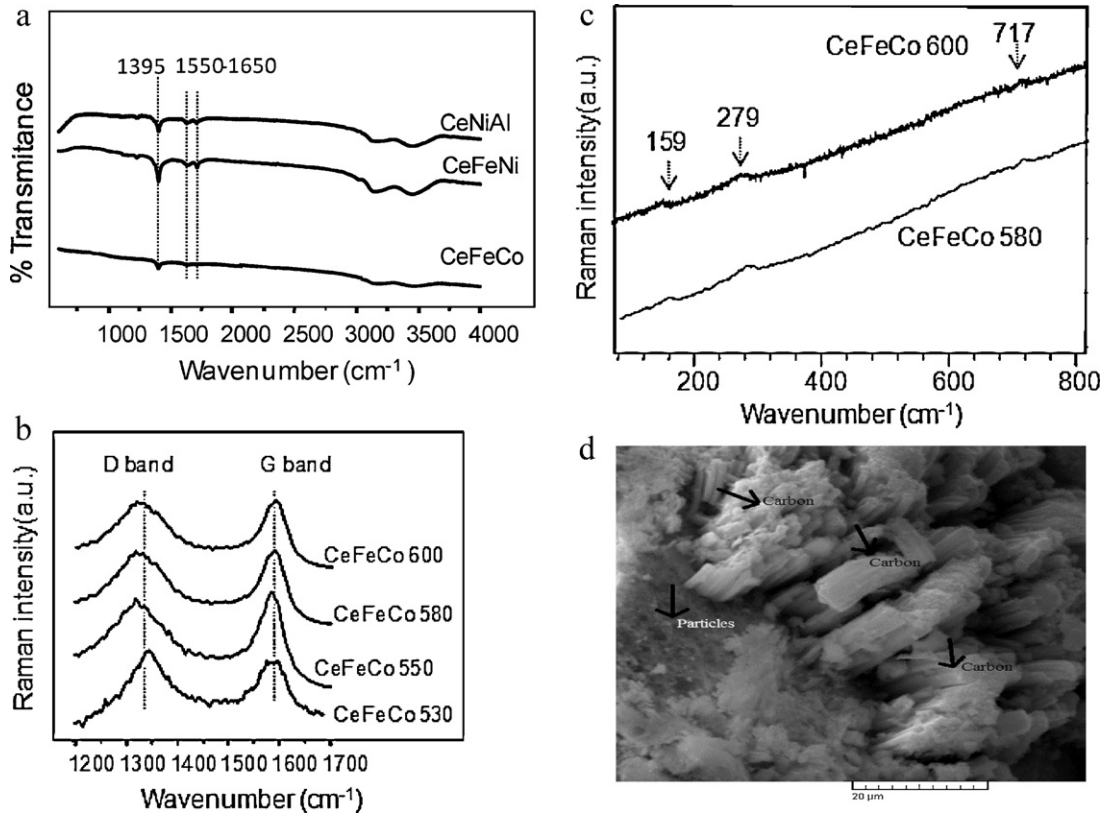

Fig. 9. (a) FTIR spectra of spent CeFeZr, CeFeNi and CeFeCo catalysts. (b) Raman spectra of CeFeCo used in the dehydrogenation of EB at different temperatures. (c) Raman spectra of CeFeCo 580 and CeFeCo 600 at low wave numbers. (d) SEM image of spent CeFeCo tested at 550 °C and CO_2/EB ratio of 30.

matic species deposited on the surface of the catalyst, respectively. The band at 1395 cm^{-1}, which was the strongest peak in the spectra of CeFeCo, was assigned to $=CH_2$ bending modes of styrene [12,22].

The FTIR results revealed that carbon was deposited on CeNiAl and CeFeNi. Alternatively, only minor amounts of coke were observed on spent CeFeCo (further confirmed by TGA results). Moreover, the Raman spectra of spent CeFeCo used at different reaction temperatures exhibited minor differences around 1100–1700 cm^{-1} (Fig. 9b).

Disorder-induced planes of carbon and graphite, known as D and G bands [49,50], respectively, were attributed to the bands at 1351 cm^{-1} and 1577 cm^{-1}. The spectra of spent CeFeCo used in the dehydrogenation of EB at 530–550 °C were obtained, and the similar intensity between the D and G bands revealed the presence of disordered carbon species (e.g., 1321 cm^{-1}); bands related to graphite (i.e., filamentous carbon species) at approximately 1587 cm^{-1} were observed, along with a amorphous carbon species. Similarly, the presence of carbon species on Fe-based catalysts has been observed in previous studies [8,13]. Furthermore, at 530–550 °C deactivation was severe because carbonaceous species were in close contact with the surface of the catalyst, as observed in a previous study [13]. As a result, CO_2 could not eliminate deposited carbon via the gasification of coke and the Boudouard reaction, and the number of active sites in the material was reduced [8,50]. This results in a modest catalyst resistance of the sample towards coking. Between 550 and 580 °C, the carbon elimination rate was probably higher than the carbon deposition rate, and the deposition of amorphous carbon on the surface of the catalyst decreased as compared to that of graphite under these conditions. Indeed, at 600 °C, both disordered and graphite carbon species were obtained; however, the mechanism of the reaction was constant, and the performance of the catalyst was superior. In other words, the Raman spectra indicated that CeFeCo possessed a stable spinel structure (e.g., $CoFe_2O_4$) which was difficult to reduce and was resistant to amorphous carbon species from EB or CO decomposition at elevated temperatures. Raman spectrum of CeFeCo displayed bands at 159, 279, and 717 cm^{-1} that are related to F2 g active phonon modes of $CoFe_2O_4$ at low wavenumbers (Fig. 9c). For CeFeCo 530 and CeFeCo 550, these bands were not visible due to the high amounts of carbon deposited at 530 and 550 °C.

The differences in the Raman spectra of the catalyst can be attributed to variations in the reaction mechanism and the amounts of coke at temperatures up to 530 °C. For instance, the amount of coke deposited was 51, 39, 24 and 17 wt%, respectively for CeFeCo 530, CeFeCo 550, CeFeCo 580, CeFeCo 600. Thus, as the temperature increased up to 550 °C, the amount of carbon formed on the catalyst decreased, and performance of the catalyst increased considerably. Moreover, at 600 °C, coke amount was limited due to the high temperatures of the reaction and the ability of CO_2 to remove carbonaceous material. As a result, equilibrium was attained at longer reactions times.

Additionally, SEM image of spent CeFeCo (Fig. 9d) exhibited nanoparticles associated with carbon deposits, which had indeed grows on the top of the particle. This means that CeFeCo, which displayed similar catalytic performance to that of traditional iron oxides obtained by co-precipitation [6,11], coking was the main cause of deactivation in the ternary composites. However, among the nanocasted oxides studied, the CeFeCo displayed increased resistance to carbon amorphous deposition and phase transformation probably due to the basic properties of CeO_2 and the stability provided by $CoFe_2O_4$ phase (from basicity measurements, TPR and Raman results). Indeed, the best catalytic performance of CeFeCo was due to the balance between the basic sites and the mesoporous features that avoid high carbon deposits at high temperatures, as

compared with the other nanocasted oxides. Although the conversions to ethylbenzene obtained over the nanocasted oxides studied were lower than the solids commercially available for the direct dehydrogenation of ethylbenzene with steam [3,4,55], the nanostructured features of the iron spinel-based oxides resulted in stable catalytic performance as compared to traditional catalysts obtained by co-precipitation [51,55].

4. Conclusions

Composite oxides were synthesised by nanocasting polymeric spherical resins. Characterisation studies revealed that binary oxides consisted of various phases such as CeO_2, SnO_2 and Mn_2O_3. Moreover, the results suggested that Fe_2O_3 was in an amorphous state or existed as nanoparticles. Most of the catalysts were perfect replicas of the mold, possessing mesostructured features and basic sites of mild to medium strength (except for SnO_2); however, the catalysts were not stable under a hydrogen atmosphere.

On the contrary, most of the ternary composite oxides were not inverse replicas of the template and possessed higher basicity and reducibility than their binary counterparts due to the stabilisation by ZrO_2 or spinel phases such as $NiAl_2O_4$ and $CoFe_2O_4$. The ternary oxide possessing $CoFe_2O_4$ phase was more active in the dehydrogenation of ethylbenzene than the binary analogues. The highest activity for styrene production was observed with CeFeCo due to the synergetic effect between $CoFe_2O_4$ and CeO_2, which promoted the RWGS reaction. Indeed, CeFeCo displayed increased resistance to carbon amorphous deposition at relatively high temperatures. Alternatively, at elevated temperatures, the cracking reactions of ethylbenzene were observed, but catalytic performance did not decreased. The effect of the structure of nanocasted oxides on the dehydrogenation of ethylbenzene was related to the nanostructured features of iron and nickel-based oxides, which provided active, stable and selective catalyst for styrene production, compared to traditional catalysts obtained by co-precipitation.

Acknowledgments

The authors wish to acknowledge to FUNCAP/UFC for the scholarship and also to funding this research.

References

[1] K.N. Rao, B.M. Reddy, B. Abhishek, Y.-H. Seo, N. Jiang, S.-E. Park, Appl. Catal. B: Environ. 91 (2009) 649–656.
[2] C. Li, C. Miao, Y. Nie, Y. Yue, S. Gu, W. Yang, W. Hua, Z. Gao, Chin. J. Catal. 31 (2010) 993–998.
[3] A.C. Oliveira, J.L.G. Fierro, A. Valentini, P.S.S. Nobre, M.C. Rangel, Catal. Today 686 (85) (2003) 49–57.
[4] R.J. Balasamya, A. Khurshida, A.A.S. Al-Ali, L.A. Atanda, K. Sagata, M. Asamoto, H. Yahiro, K. Nomura, T. Sano, K. Takehira, S.S. Al-Khattaf, Appl. Catal. A: Gen. 390 (2010) 225–234.
[5] W. Bieniasz, M. Trebala, Z. Sojka, A. Kotarba, Catal. Today 154 (2010) 224–228.
[6] A. Sun, Z. Qin, S. Chen, J. Wang, J. Mol. Catal. A: Chem. 210 (2004) 189–195.
[7] C.L. Lima, O.S. Campos, A.C. Oliveira, F.F. de Sousa, J.M. Filho, P.L. Neto, A.N. Correia, G.Q. Sabadia, I.M. Nogueira, G.S. Pinheiro, A.C. Oliveira, Appl. Catal. A: Gen. 395 (2011) 53–63.
[8] A.H.M. Batista, F.F. de Sousa, S.B. Honorato, A.P. Ayala, J.M. Filho, F.W. de Sousa, A.N. Pinheiro, J.C.S. de Araujo, R.F. Nascimento, A. Valentini, A.C. Oliveira, J Mol. Catal. A: Chem. 315 (2010) 86–98.
[9] J.J. Delgado, X. Chen, J.P. Tessonnier, M.E. Schuster, E. Del Rio, R. Schlogl, D.S. Su, Catal. Today 105 (2010) 49–54.
[10] C. Wang, W.-B. Fan, Z.-T. Liu, J. Lu, Z.-W. Liu, Z.-F. Qin, J.-G. Wang, J. Mol. Catal. A: Chem. 239 (2010) 64–70.
[11] J.C.S. Araujo, F.N.A. Freire, C.B.A. Souza, A.C. Oliveira, A.P. Ayala, A.C. Oliveira, Appl. Catal. A: Gen. 377 (2010) 55–63.
[12] R.M. Freire, F.F. de Sousa, A.L. Pinheiro, E. Longhinotti, J.M. Filho, A.C. Oliveira, P.T.C. Freire, A.P. Ayala, A.C. Oliveira, Appl. Catal. A: Gen. 359 (2009) 165–179.
[13] H.E.M. Batista, F.S.O. Ramos, T.B. Pinheiro, C.L. Lima, F.F. de Sousa, E.B.D. Barros, J.M. Filho, A.S. de Oliveira, J.R. de Souza, A. Valentini, A.C. Oliveira, Appl. Catal. A: Gen. 382 (2010) 148–157.
[14] B.S. Liu, R.Z. Chang, L. Jiang, W. Liu, C.T. Au, J. Phys. Chem. C 112 (2009) 15490–15501.
[15] Y.G. Wang, Y.Q. Wang, Y. Guo, Y.L. Guo, X.H. Liu, G.Z. Lu, Stud. Surf. Sci. Catal. 165 (2007) 361–364.
[16] J. -H, N. Smått, M. Schuwer, W. Jarn, M. Lindner, Lindén, Micropor. Mesopor. Mater. 112 (2008) 308–318.
[17] D.-W. Lee, C.-Y. Yu, K.-H. Lee, Mater. Chem. Phys., doi:10.1016/j.matchemphys.2010.04.033, in press.
[18] S. Lepoutre, J.-H Smått, C. Laberty, H. Amenitsch, D. Grosso, M. Lindén, Micropor. Mesopor. Mater. 123 (2009) 185–192.
[19] X. Cui, J. Zhou, Z. Ye, H. Chen, L. Li, M. Ruan, J. Shi, J. Catal. 270 (2010) 310–317.
[20] T. Valdès-Solis, A.B. Fuertes, Mater. Res. Bull. 41 (2006) 2187–2197.
[21] M. Abecassis-Wolfovich, M.V. Landau, A. Brenner, M. Herskowitz, J. Catal. 247 (2007) 201–213.
[22] Y. Wang, X. Yuan, X. Liu, J. Ren, W. Tong, Y. Wang, G. Lu, Solid State Sci. (2008) 1117–1123.
[23] F. Arena, G. Trunfio, J. Negro, L. Spadaro, Appl. Catal. B: Environ. 85 (2008) 40–47.
[24] P. Madhusudhan Rao, P. Goldberg-Oppenheimer, S. Kababya, S. Vega, M.V. Landau, J. Mol. Catal. A: Chem. 275 (2007) 214–227.
[25] T. Garcia, S. Agouram, J.F. Sánchez-Royo, R. Murillo, A.M. Mastral, A. Aranda, I. Vázquez, A. Dejoz, B. Solsona, Appl. Catal. A: Gen. 386 (2010) 16–27.
[26] Y. Xia, H. Dai, L. Zhang, J. Deng, H. He, C.T. Au, Appl. Catal. B: Environ. 100 (2010) 229–237.
[27] P.M. Rao, P. Goldberg-Oppenheimer, S. Kababya, S. Vega, M.V. Landau, J. Mol. Catal. A: Chem. 275 (2007) 214–227.
[28] A.S. Deshpande, N. Pinna, M. Antonietti, M. Niederberg, Chem. Mater. 16 (2004) 2599–2603.
[29] L. Zhou, W.Z. Wang, S.W. Liu, L.S. Zhang, H.L. Xu, W. Zhu, J. Mol. Catal. A: Chem. 252 (2006) 120–124.
[30] A.-H. Lu, F. Schüth, Adv. Mater. 18 (2006) 1793–1805.
[31] X. Lai, H. Wang, D. Mao, N. Yang, J. Yao, C. Xing, D. Wang, X. Li, Mater. Lett. 62 (2008) 3868–3871.
[32] S. Damyanova, B. Pawelec, K. Arishtirova, M.V. Martinez Huerta, J.L.G. Fierro, Appl. Catal. B: Environ. 82 (2009) 149–159.
[33] J. Kaspar, P. Fornasiero, M. Graziani, Catal. Today 50 (1999) 285–290.
[34] A.S. Deshpand, M. Niederberg, Micropor. Mesopor. Mater. 101 (2007) 413–418.
[35] J. Zhu, Q. Gao, Micropor. Mesopor. Mater. 124 (2009) 144–152.
[36] F. Schutz, Chem. Mater. 13 (2001) 3184–3195.
[37] H. Li, S. Zhu, H. Xi, R. Wang, Micropor. Mesopor. Mater. 89 (2006) 196–203.
[38] L.E. Smart, E.A. Moore, Solid State Chemistry – An Introduction, 3rd edition, CRC Press, New York, 2005, pp. 34–107.
[39] H.-Y. Lin, Y.-W. Chen, C. Li, Thermochim. Acta 400 (2003) 61–67.
[40] Y. Wen, X. Tang, J. Li, J. Hao, L. Wei, X. Tang, Catal. Commun. 10 (2009) 1157–1160.
[41] G. Jacobs, U.M. Graham, E. Chenu, P.M. Paterson, A. Dozier, B.H. Davis, J. Catal. 229 (2005) 499–512.
[42] B. Puertolas, B. Solsona, S. Agouram, R. Murillo, A.M. Mastral, A. Aranda, S.H. Taylor, T. Garcia, Appl. Catal. B: Environ. 93 (2010) 395–405.
[43] J. Roggenbuck, H. Schafer, T. Tsoncheva, C. Minchev, J. Hanss, M. Tiemann, Micropor. Mesopor. Mater. 101 (2007) 335–341.
[44] L. Wan, X. Cui, H. Chen, J. Shi, Mater. Lett. 64 (2010) 1379–1382.
[45] M. Rumyantseva, V. Kovalenko, A. Gaskov, E. Makshina, V. Yuschenko, I. Ivanova, A. Ponzoni, G. Faglia, E. Comini, Sens. Actuators B: Chem. 118 (2006) 208–214.
[46] E. Manova, T. Tsoncheva, C. Estournès, D. Paneva, K. Tenchev, I. Mitov, L. Petrov, Appl. Catal. A: Gen. 300 (2006) 170–180.
[47] S.S.-Y. Lin, D.H. Kim, M.H. Engelhard, S.Y. Ha, J. Catal. 273 (2010) 229–235.
[48] G. Neri, A. Bonavita, G. Rizzo, S. Galvagno, S. Capone, P. Siciliano, Sens. Actuators B: Chem. 111 (2005) 78–83.
[49] A.N. Pinheiro, J.M. Sasaki, A. Valentini, A.C. Oliveira, Appl. Catal. A: Gen. 355 (2009) 156–168.
[50] A.L. Pinheiro, A.N. Pinheiro, A. Valentini, J.M. Filho, F.F. de Sousa, J.R. de Sousa, M.G.C. Rocha, P. Bargiela, A.C. Oliveira, Catal. Commun. 11 (2009) 11–14.
[51] S.M. Saito, H. Mimura, N.W. Kimura, J.K. Murata, Appl. Catal. A: Gen. 239 (2003) 71–77.
[52] X.M. Zhu, M. Schön, U. Bartmann, A.C. van Veen, M. Muhler, Appl. Catal. A: Gen. 266 (2004) 99–108.
[53] R.J. Balasamy, B.B. Tope, A. Khurshid, A.A.S. Al-Ali, L.A. Atanda, K. Sagata, M. Asamoto1, H. Yahiro, K. Nomura, T. Sano, K. Takehira, S.S. Al-Khattaf, Appl. Catal. A: Gen. 396 (2011) 107–115.
[54] A. Trovarelli, C. Leitenburg, M. Boaro, G. Dolcetti, Catal. Today 50 (1999) 353–367.
[55] A. Sun, Z. Qin, J. Wang, Appl. Catal. A: Gen. 234 (2002) 179–189.